doi:10.1016/j.jmb.2009.12.007 J. Mol. Biol. (2010) 396, 761–772

JMB

Available online at www.sciencedirect.com

ScienceDirect

ELSEVIER

Discrimination between Closely Related Cellular Metabolites by the SAM-I Riboswitch

Rebecca K. Montange, Estefanía Mondragón, Daria van Tyne, Andrew D. Garst, Pablo Ceres and Robert T. Batey*

Department of Chemistry and Biochemistry, University of Colorado, Boulder, Campus Box 215, Boulder, CO 80309-0215, USA

Received 18 August 2009; received in revised form 30 November 2009; accepted 6 December 2009
Available online
16 December 2009

The SAM-I riboswitch is a cis-acting element of genetic control found in bacterial mRNAs that specifically binds *S*-adenosylmethionine (SAM). We previously determined the 2.9-Å X-ray crystal structure of the effector-binding domain of this RNA element, revealing details of RNA–ligand recognition. To improve this structure, variations were made to the RNA sequence to alter lattice contacts, resulting in a 0.5-Å improvement in crystallographic resolution and allowing for a more accurate refinement of the crystallographic model. The basis for SAM specificity was addressed by a structural analysis of the RNA complexed to *S*-adenosylhomocysteine (SAH) and sinefungin and by measuring the affinity of SAM and SAH for a series of mutants using isothermal titration calorimetry. These data illustrate the importance of two universally conserved base pairs in the RNA that form electrostatic interactions with the positively charged sulfonium group of SAM, thereby providing a basis for discrimination between SAM and SAH.

Keywords: non-protein-coding RNA; X-ray crystallography; isothermal titration calorimetry; riboregulation; *S*-adenosylmethionine

Edited by J. Doudna

Introduction

Riboswitches are non-protein-coding elements found in mRNAs that directly bind a metabolite to regulate the transcript's expression.[1] Of the more than 20 riboswitch families identified to date, one of the most prevalent responds to *S*-adenosylmethionine (SAM), regulating a broad assortment of genes involved in sulfur metabolism.[2] This family is represented by five classes of RNAs (SAM-I, SAM-II, SAM-III, SAM-IV, and SAM-V), each defined by a distinct pattern of sequence conservation.[2–8] Three of these classes (SAM-I, SAM-II, and SAM-III) have fundamentally different folds as revealed by X-ray crystallography,[9–11] implying that they represent evolutionarily independent solutions to SAM recognition by RNA.[2]

Members of the SAM riboswitch family all bind SAM with high affinity and selectivity over *S*-adenosylhomocysteine (SAH),[2] the product of enzymatic reactions that use SAM as a methyl group donor. Since SAM serves as the primary methyl donor for most biological methylation reactions and SAH is toxic at high intracellular concentrations,[12] it is crucial that proteins and RNAs involved in regulation of cellular SAM/SAH ratios efficiently discriminate between these two compounds.[2] Specificity of the SAM-binding riboswitches is thought to arise from a potential electrostatic interaction between the RNA and the positively charged sulfonium moiety of SAM (Fig. 1),[2,13] a feature absent from SAH, which contains a neutral sulfoether (Fig. 1). Given the interest in riboswitches as potential therapeutic targets,[13,14] it is critical to understand how they achieve their high degree of selectivity in order to design new molecules that mimic these recognition elements.

A recent crystal structure of the *Thermoanaerobacter tengcongensis* (*Tte*) *metF-H2* SAM-I riboswitch illuminated the molecular basis for SAM recognition as well as a possible mechanism for discrimination

*Corresponding author. E-mail address: Robert.Batey@colorado.edu.

Present address: R. K. Montange, JILA/NIST, University of Colorado, Boulder, CO 80309-0440, USA; D. van Tyne, Department of Immunology and Infectious Disease, Harvard School of Public Health, Boston, MA 02115, USA.

Abbreviations used: ITC, isothermal titration calorimetry; SAH, *S*-adenosylhomocysteine; SAM, *S*-adenosylmethionine; SFG, sinefungin; MPD, methyl-2,4-pentanediol; PDB, Protein Data Bank.

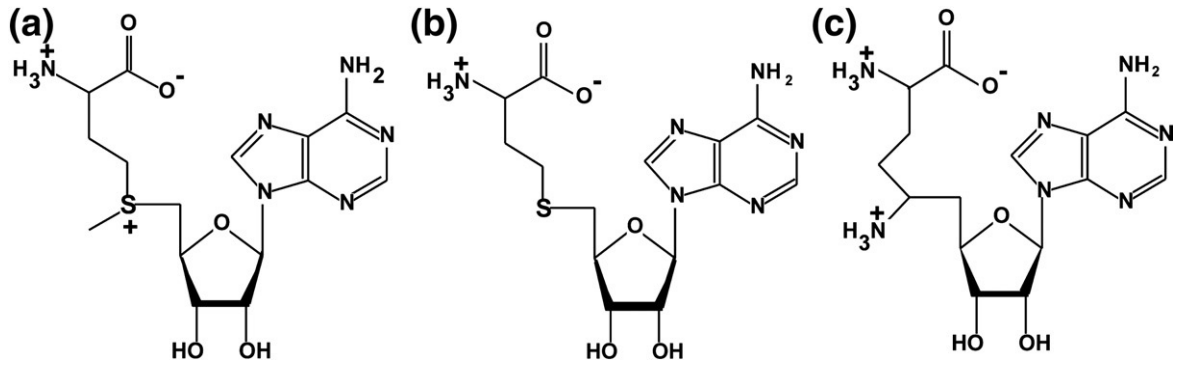

Fig. 1. Chemical structure of (a) SAM, (b) SAH, and (c) SFG.

against SAH.[9] This 2.9-Å-resolution model revealed that this RNA comprises two sets of coaxially stacked helices (P1/P4 and P2/P3) organized around a four-way junction. SAM binds within a bipartite pocket formed between the minor grooves of helices P1 and P3 in a cis conformation such that the methionine moiety is stacked upon the adenosyl ring. This configuration positions the methionine main-chain atoms and adenosyl moiety of SAM to form hydrogen bonds primarily with an internal loop in P3. The positively charged sulfonium ion forms an electrostatic interaction with the carbonyl oxygens of two universally conserved A–U pairs (A6–U88 and U7–A87)[2,5,15] in the minor groove of P1, augmented by van der Waals interactions with the ribose moiety.[9] However, the moderate resolution of the data and local regions of poorly defined electron density led to ambiguities in modeling certain features of the RNA. Furthermore, the role of cations in stabilizing the overall fold of the RNA was unaddressed.

To further our understanding of this regulatory element, we sought to obtain higher-resolution crystallographic data to improve our model of the riboswitch. By testing a series of sequence variants of the RNA originally crystallized, we identified a double mutant that yielded crystals that extended the diffraction limit of our data to 2.4 Å resolution in complex with SAM, allowing us to model the atomic details of the SAM-I riboswitch with greater confidence. In addition, this RNA was crystallized in complex with SAH and sinefungin (SFG), chemical analogs of SAM (Fig. 1), to elucidate a structural basis for discrimination. However, the resulting structures reveal almost identical patterns of RNA–ligand contacts as observed for SAM.

As an alternative approach to understanding specificity for SAM, mutations that alter the two universally conserved base pairs in the P1 helix implicated in recognizing the sulfonium group of SAM were introduced. Measurement of the binding affinities of each mutant for SAM and SAH by isothermal titration calorimetry (ITC) revealed that while alterations of the A–U pairs strongly affect the RNA's affinity for SAM, they have negligible effects on SAH binding affinity. Structural analysis of the most deleterious of these mutants shows that SAM occupies a nearly identical position as in the wild-type RNA, resulting in nonoptimal electrostatic interactions. Together, our structural data suggest that the ligand cannot readjust the position of the sulfonium ion in the binding pocket to reestablish favorable interactions. Furthermore, these findings strongly support the idea that this key electrostatic interaction between SAM and the RNA drives the riboswitch's selectivity.

Results and Discussion

Designing and crystallizing lattice contact variants

In our original structural analysis of the *Tte*SAM-I riboswitch, the helical lengths of P1, P3, and P4 were varied in length, and the sequence composition of non-conserved loops was altered to obtain an RNA that yielded crystals that diffracted X-rays to 2.9 Å.[9,16] To find RNAs that potentially would yield crystals that diffract to higher resolution, we identified six intermolecular contacts in the original structure and introduced point mutations to residues that either form the contacts or participate in base pairs immediately adjacent to these sites in an attempt to positively influence lattice formation. This is a commonly employed strategy in protein crystallography[17–19] and one that has proven useful for other RNAs.[20–24] A detailed discussion of the lattice contacts, variants introduced into the RNA, crystallization conditions, and the impact of alterations on crystallizability is available in Supplementary Materials (Supplemental Discussion, Tables S1 and S2; Figs. S1 and S2). A small sample of these variants, two of which crystallized (A94G and A94G/U34C) and one of which did not (A75G), were assayed for SAM binding by ITC and were found to bind with equivalent affinity to the parent construct (Table S3). The most successful variant, A94G/U34C, contained alterations to two residues involved in intermolecular contacts and was found to diffract to 2.4 Å using both in-house and synchrotron X-ray sources. This RNA also crystallized well in the presence of the physiologically relevant divalent magnesium, allowing for the role

of cations to be addressed. The resulting data yielded a model at 0.5 Å higher resolution than previously reported with good refinement statistics (R/R_{free} = 20.4%/26.2%). Crystallographic statistics are reported in Table 1.

New details from the SAM-I structure at 2.4 Å resolution

The overall global architecture of the *Tte*(U34C/A94G)SAM-I variant is identical with that previously reported; however, with improved resolution, the fine structure of local regions can be more reliably modeled. For example, a better determination of sugar puckers within the kink-turn motif was the result of the higher quality of electron density in this region (Fig. S3). In our original model, U34 was modeled with a C3′-*endo* sugar pucker. This is inconsistent with the C2′-*endo* pucker typically observed in kink-turns that allows for the formation of an important hydrogen bond between its 2′-hydroxyl group and an adjoining non-bridging oxygen within the backbone.[25] In the newly refined model, this sugar is clearly in a C2′-*endo* conformation, allowing this key interaction to be formed (Fig. 2a). Furthermore, both G35 and G19 are in a C2′-*endo* conformation, allowing for additional hydrogen-bonding interactions between the 2′-hydroxyl group of G35 to N2 of G19 and the 2′-hydroxyl group of G19 to the adjacent non-bridging oxygen of the 5′-phosphate. Although these newly observed interactions are atypical, there is precedence for structural plasticity in the kink-turn motifs of other RNAs, including a highly unusual motif identified in a recent crystal structure of the lysine riboswitch.[25–27]

Another improved aspect of our model is the definition of the electron density about the SAM ligand in the final $2F_o - F_c$ map. With this improved density, it is clear that the SAM ribose sugar adopts a C3′-*endo* pucker (Fig. 2b). As in the previously reported structure, SAM's 3′-hydroxyl group does not interact with the RNA while the 2′-hydroxyl group hydrogen bonds to O4′ in C47.[9] Furthermore, the position of the methionine main chain of SAM is better defined, such that these atoms are slightly rotated to position the methionine carboxyl group coplanar with G11, as opposed to the more twisted interaction previously reported (Fig. 2c).[9] Additionally, the ribose sugar of A46, one of three nucleotides in the asymmetric internal loop of P3 that directly interacts with SAM, is now modeled in a C2′-*endo* where previously it was C3′-*endo*. Together, these improvements lead to a more accurate model of the ligand-binding pocket of the RNA and also reveal potential conformational flexibility in the J1/2 linker region (see Supplementary Materials).

As a final step in refining our model, we were able to place eight magnesium ions that illuminate the structural roles of metals (Fig. 3a; numbered as they appear from the 5′ to 3′ ends). A number of these ions are found at positions likely to be important for establishing the proper architecture of the RNA, although none of them directly coordinate the SAM ligand. For example, Mg-1 bridges J1/2 and J3/4 through coordinated waters (Fig. 3b), while Mg-3

Table 1. Crystallographic statistics for data collection and model refinement

RNA:ligand	A94G/U34C:SAM	A94G/U34C:SAM in $MnCl_2$	A94G/U34C:SAH	A94G/U34C:SFG	A94G/U34C/A6C–U88G/U7G–A87C:SAM (GC-SAM)
Data collection					
Wavelength (Å)	1.0809	1.5418	1.5418	1.5418	1.5418
Space group	$P4_32_12$	$P4_32_12$	$P4_32_12$	$P4_32_12$	$P4_32_12$
Cell dimensions					
$a=b$, c (Å); $\alpha=\beta=\gamma$ (°)	62.7, 158.6; 90	62.3, 159; 90	62.4, 158.2; 90	62.6, 158.4; 90	62.6, 159.6; 90
Resolution (Å)	20–2.4 (2.5–2.4)[a]	20–2.8 (2.9–2.8)	19.7–2.7 (2.8–2.7)	19.8–2.9 (3.0–2.9)	20–2.95 (3.06–2.95)
R_{merge}[b]	0.051 (0.548)	0.092 (0.387)	0.075 (0.369)	0.059 (0.369)	0.068 (0.439)
$I/\sigma I$	20.7 (2.4)	9.5 (3.3)	15.7 (4.6)	15 (3.7)	13.3 (3.7)
Completeness (%)	98.3 (87.4)	87.9 (91.6)	98.3 (97.6)	99.4 (100)	99.6 (100)
Measured reflections	210,152	26,255	60,653	42,053	47,654
Unique reflections	12,862	7215	8993	7451	7157
Redundancy	16.4 (8.4)	3.6 (3.6)	6.74 (7.06)	5.64 (5.53)	6.66 (6.81)
Refinement[c]					
Resolution (Å)	19.8–2.4	18.5–2.8	19.7–2.7	19.4–2.9	20–2.95
No. of reflections					
Working set	10,486	6329	8080	6604	6335
Test set	1166	707	897	779	705
R_{work}/R_{free}[d]	20.4/26.2	26/32.7	23.2/28.7	22.2/28.7	22.1/27.5
Average B-factors (Å^2)	64.67	62.28	54.6	68.1	80.7
Maximum likelihood coordinate error (Å)	0.37	0.55	0.53	0.36	0.55
rmsd bond lengths (Å)	0.005	0.003	0.006	0.003	0.004
rmsd bond angles (°)	1.19	0.88	2.5	2.17	1.87
PDB ID	3GX5	3GX6	3GX3	3GX2	3GX7

[a] Values for the highest resolution shell are shown in parentheses.
[b] $R_{merge} = \sum|I - \langle I\rangle| / \sum I$.
[c] Refinement was against all data within the stated resolution range, with a random 10% omitted for use in calculation of R_{free}.
[d] $R_{xtal} = \sum||F_o| - |F_c|| / \sum|F_o|$ for the working set. R_{free} is the same for the test set.

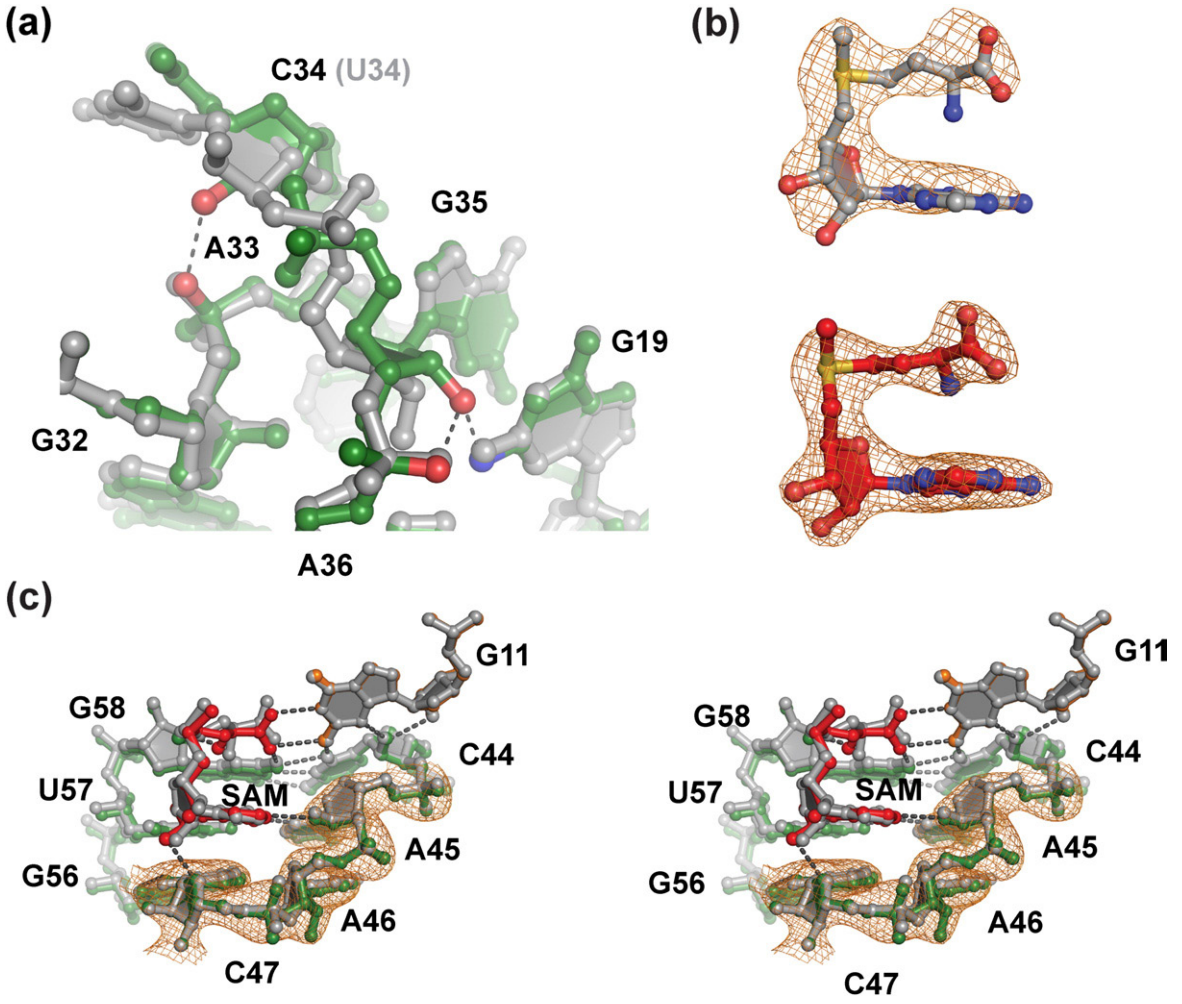

Fig. 2. (a) Overlay of the kink-turn motif in the original *Tte*SAM-I (gray, PDB ID: 2GIS[9]) and *Tte*(A94G/U34C)SAM-I (green) structures. New hydrogen bonds in the kink-turn are shown as black dashes. An important backbone–backbone contact between C34 and A33 is now observed. (b) Comparison of the electron density (orange mesh, $2F_o - F_c$ density map contoured to 1 σ) surrounding the SAM ligand in the original *Tte*SAM-I (top) and the *Tte*(A94G/U34C)SAM-I (bottom) structures. Note the improved density about the methionine moiety and improved definition about the ribose in the latter structure. (c) Stereoview of the P3 side of the binding pocket. The *Tte*SAM-I (gray) and the *Tte*(A94G/U34C)SAM-I (colored) are overlaid to show that the only notable change is the changed sugar pucker of A46. Hydrogen bonds in the binding pocket are depicted as gray dashes. Electron density from the refined *Tte*(A94G/U34C)SAM-I $2F_o - F_c$ density map contoured to 1 σ is drawn about C47, A46, and A45.

lies adjacent to the kink-turn, which is known to bind divalent ions with high affinity.[28] Other important cations are found adjacent to the SAM-binding pocket (Mg-5) and within the core of the RNA (Mg-6). Mg-5 sits adjacent to the A46·C47–G56 triple and A45–A46 stack, on the major groove side of the SAM-binding pocket (Fig. 3c). Mg-6 is positioned near a critical tertiary interaction between J4/1, J3/2, and L2 (A85, U64, and A24, respectively) via contacts with its coordinated waters and A24(N7) and the 2′-hydroxyl group of U64 (Fig. 3d). This magnesium also coordinates with bases involved in the J3/4 strand of the pseudoknot. The positions of these magnesium ions were validated using manganese-soaked crystals (Table 2; Fig. 3e) and were also consistent with barium binding sites observed in variant A94G in both the liganded and unliganded states (data not shown). In addition, one potassium ion was modeled adjacent to the U5·G89 wobble pair in the P1 helix, which was validated using a cesium soak (data not shown).

SAM analogs bind to the riboswitch in a structurally similar fashion

Like its protein counterparts, a critical aspect of the SAM-I riboswitch's proper regulation of SAM biosynthesis is the ability to sense the SAM/SAH ratio in the cell by selectively binding SAM. We previously proposed that SAM-I discriminates between SAM and SAH via two universally conserved A–U pairs in the P1 helix that position two carbonyl oxygens [U7(O2) and U88(O2)] adjacent to the positively charged sulfonium ion, to form an energetically favorable electrostatic interaction (Fig. 4a).[9] It is noteworthy that the SAM-II and

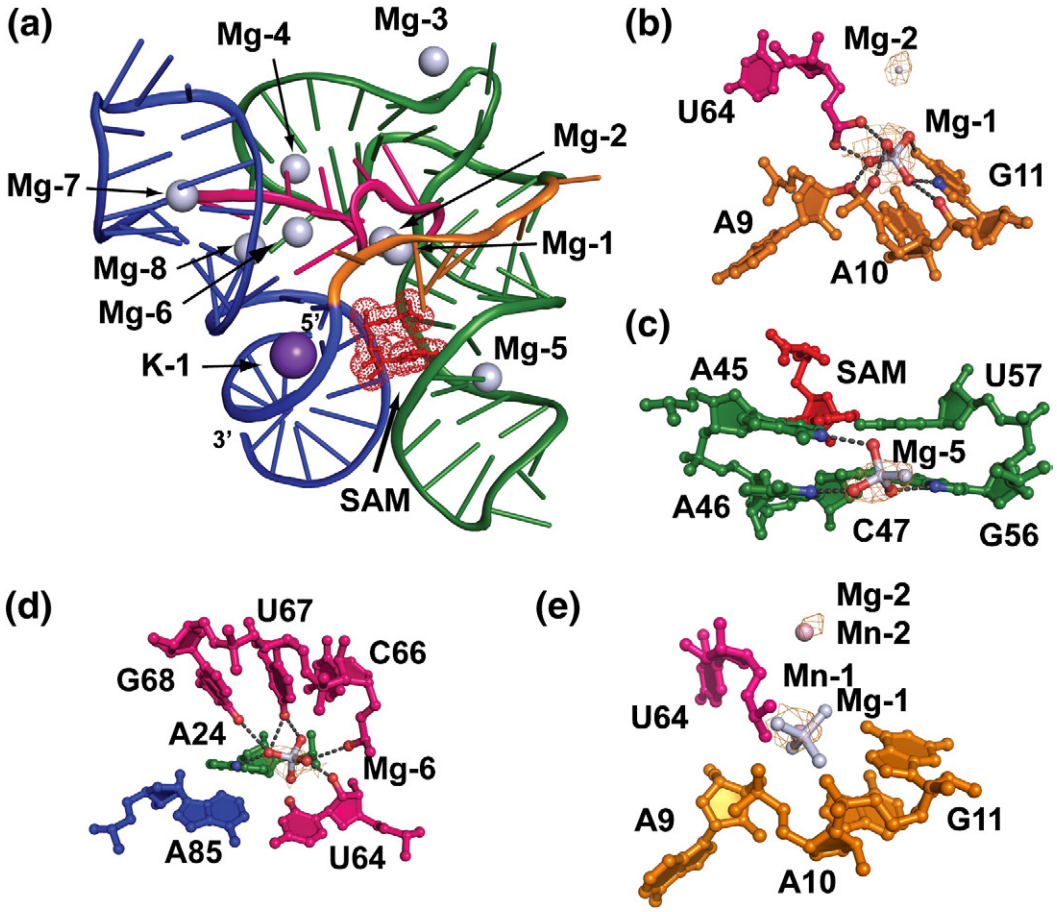

Fig. 3. (a) Metals mapped onto the global structure (PDB ID: 3GX5). Magnesium is light blue and potassium is purple. Helices P1 and P4 are colored blue and helices P2 and P3 are green. Joining regions J1/2 and J3/4 are orange and magenta, respectively. (b) The contacts made by the magnesium ions (light blue) in J1/2 (orange) and J3/4 (magenta). The waters of hydration are red and outer sphere coordinations are shown as gray dashes. Atoms involved in the interactions are colored red (oxygen) and blue (nitrogen). The orange mesh represents the $2F_o - F_c$ map contoured to 1.2 σ. (c) The magnesium involved in the A46·C47–G56 triple (green). SAM (red) is in the background but does not interact with this magnesium. (d) The magnesium involved in mediating the A24 (green)·A85 (blue)–U64 (magenta) triple and stabilizing the J3/4 strand of the pseudoknot (magenta). (e) Manganese and magnesium in J1/2 (orange) and J3/4 (magenta). Magnesium is pale blue with the waters of hydration in red. Manganese is pink. The orange mesh represents the $2F_o - F_c$ map calculated for the manganese data set (PDB ID: 3GX6). Contour level is 1.5 σ.

SAM-III riboswitches, despite highly divergent folds and differences in the conformation and recognition of the ligand, also position the sulfonium group adjacent to carbonyls in the binding pocket.[10,11] Biochemical studies have shown that SAH and SFG (Fig. 1) respectively bind ~100 and ~180-fold more weakly than SAM[5,17] while SAM analogs bearing a positive charge such as a quaternary amine at the site of SAM's sulfonium moiety bind SAM-I with equal affinity,[13] indicating that both the presence and position of the positive charge are critical for achieving maximal affinity.

To determine if the loss of this interaction alters the position of ligand in the binding pocket, we solved the structure of SAM-I bound to SAH to 2.7 Å resolution (Table 1). SAH forms the same set of hydrogen-bonding interactions with P3 (Fig. S5a and b) and places the neutral sulfur atom at the same position as the sulfonium ion of SAM, which is within the coordinate error of both models (Fig. 4b; Table 1). Thus, van der Waals interactions between the ribose sugar and sulfur atom and P3 likely serve as the principal means of orienting the ligand in the binding pocket, and the electrostatic interaction further stabilizes the resulting complex (see below).

*Tte*SAM-I was also crystallized in the presence of SFG to determine whether this antimicrobial and antifungal agent would also bind in a similar fashion (Table 1). Despite bearing a positive charge at a nearly identical position as SAM (Fig. 1), SFG has reduced binding affinity,[13] indicative of a weaker interaction with the RNA. The model of this complex was refined to 2.9 Å, revealing that the adenosyl and amino acid main-chain moieties of SFG form the same set of hydrogen bonds observed in the SAM and SAH structures (Fig. S5c). In this model, we observed that the position of the carbon and primary amine is also not altered relative to the equivalent sulfur and methyl group in SAM (Fig. 4c). The inability of the ligand to adjust its position

Table 2. Dissociation constant data for P1 mutants of *Tte*SAM-I

P1 sequence[a]	$K_{d,SAM}$ (μM)	$K_{d,REL}$ (mut/wt)-SAM[b]	$K_{d,SAH}$ (μM)	$K_{d,REL}$ (mut/wt)-SAH[c]	$K_{d,REL}$ (SAH/SAM)[d]
U7–A87 A6–U88	0.13±0.01	1	71±2	1	550
A7–U87 U6–A88	2.1±0.1	16	n.d.[e]	n.d.	n.d.
A7–U87 A6–U88	2.3±0.4	18	n.d.	n.d.	n.d.
U7–A87 U6–A88	0.91±0.05	7	75±3	1.1	36
C7–G87 G6–C88	3.3±0.4	25	74±7	1.0	22
G7–C87 C6–G88	31±1	240	82±2	1.2	2.6
G7–C87 G6–C88	24±3	190	n.d.	n.d.	n.d.
C7–G87 C6–G88	4.6±0.2	35	68±1	1	15

[a] The first RNA in this series (U7–A87/A6–U88) represents the wild-type sequence and subsequent sequences represent the mutations to this sequence.
[b] $K_{d,REL}$(mut/wt)-SAM = K_d(mutant RNA, SAM)/K_d(wild-type RNA, SAM).
[c] $K_{d,REL}$(mut/wt)-SAH = K_d(mutant RNA, SAH)/K_d(wild-type RNA, SAH).
[d] $K_{d,REL}$(SAH/SAM) = K_d(RNA, SAH)/K_d(RNA, SAM).
[e] n.d., not determined.

to optimize the electrostatic interaction suggests a rigid binding pocket that does not allow for significant adaptive binding, in contrast to what has been observed in other riboswitches.[29–31]

To further assess potential differences in binding between SAM and its chemical analogs to the SAM-I riboswitch, we examined the ordering of ligands in the binding pocket using a *B*-factor analysis. Although differences in the resolution and unit cell size can make direct comparisons of *B*-factors difficult, if the *B*-factors are normalized, some comparisons can be made.[32–34] For the structures presented in this work, the *B*-factors were normalized according to the equation

$$B_{norm} = \frac{(B - \langle B \rangle)}{\sigma_B} \quad (1)$$

where B_{norm} is the normalized *B*-factor, B is the experimental *B*-factor, $\langle B \rangle$ is the average *B*-factor for the structure, and σ_B is the standard deviation.[32–34] While both SFG and SAH are well defined by electron density (Fig. 4d), their normalized *B*-factors are slightly higher than that of SAM (Fig. 4e). This suggests, particularly for SFG, that the ligands are more disordered within the binding pocket, reflective of their lowered binding affinities. In contrast, normalized *B*-factors for the RNA between the three models show few differences (Fig. S6).

The role of electrostatic contacts in SAM specificity

To further probe the importance of the SAM–P1 helix electrostatic interaction for binding and selectivity, we constructed a series of mutations of the universally conserved U7–A87 and A6–U88 base pairs. It was reasoned that transversions of either one or both of these pairs would create suboptimal arrangements between the sulfonium cation and carbonyl oxygens in the minor groove. Mutants were also made in which the A–U pairs were converted to G–C pairs, altering the electrostatic surface potential of the minor groove by introducing a partial positive charge carried by the exocyclic amine of guanosine. The effects of these mutations on ligand binding and specificity were assessed by determining the apparent equilibrium dissociation constants (K_d) for both SAM and SAH by ITC (Table 2); representative data are shown in Fig. S7.

These experiments reveal several trends in the RNA's ability to bind SAM and discriminate against SAH. The wild-type RNA binds SAH ~550-fold more weakly than SAM (Table 1), a difference that directly reflects the loss of the positive charge on the sulfur and the methyl group. Comparison of SAM binding to the A–U transversion mutations reveals that these two pairs are not equally important in determining affinity. The U7A–A87U mutation decreased the affinity by ~18-fold while the A6U–U88A change dropped affinity by ~7 fold (Table 2). Although the structural data show that the sulfonium group is equidistant from the O2 carbonyls of U7 and U88 (Fig. 4), these ITC data suggest that the carbonyl on U7 makes a greater contribution to binding. Notably, the SAM-IV riboswitch, which is proposed to have a binding pocket nearly identical with that of SAM-I, contains a G–C pair at the position analogous to the A6–U88 pair in SAM-I.[8] Changing the orientation of both the A6–U88 and U7–A87 pairs results in an ~16-fold drop in affinity, significantly less that the ~550-fold difference in affinity between SAM and SAH. Positioning of the carbonyl groups in the minor groove of P1 is therefore important, but suboptimal electrostatic interactions still contribute substantially to affinity compared to their complete absence.

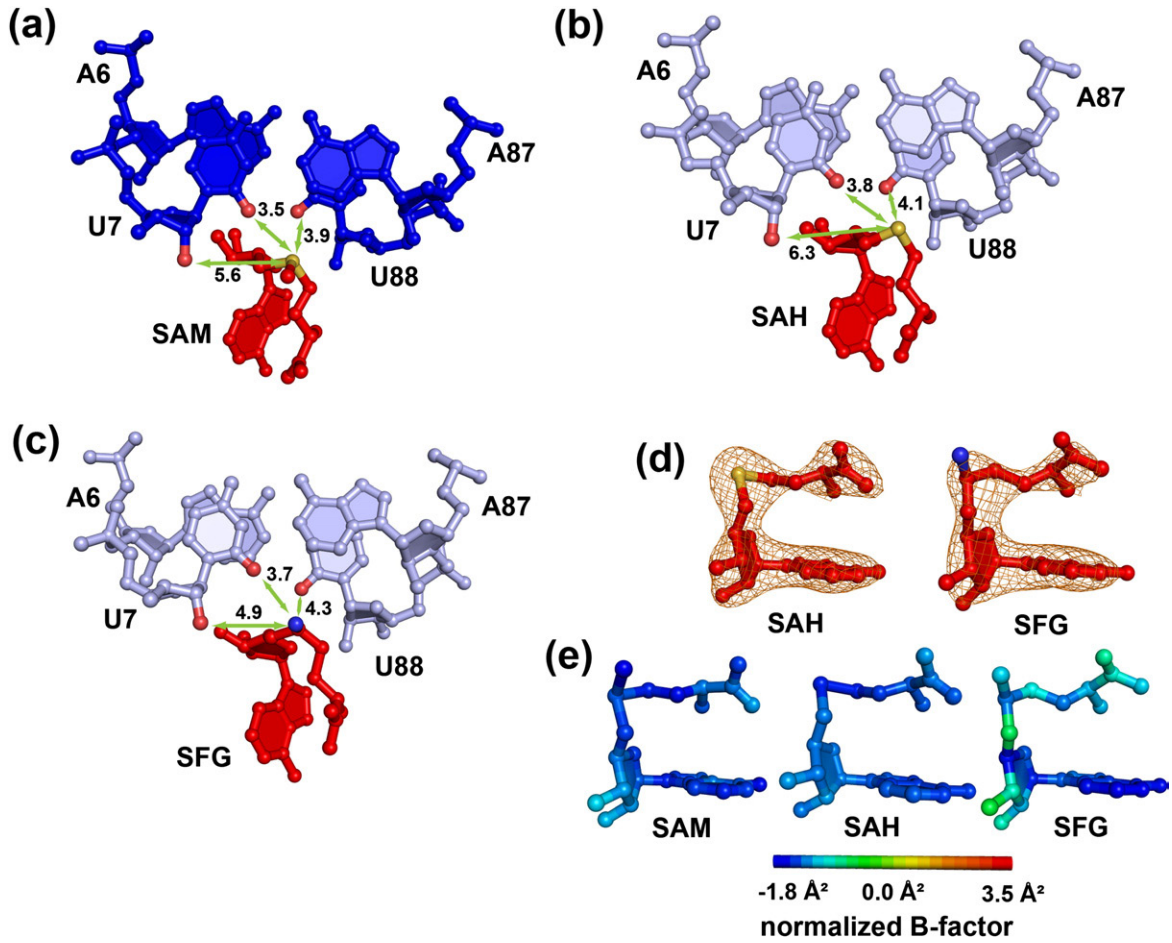

Fig. 4. (a) The interaction (green arrows) of SAM (red) with the P1 helix (blue). Distances for the electrostatic interaction are labeled. Atoms involved in the interactions are colored; oxygen is red and sulfur is yellow (PDB ID: 3GX5). (b) The interaction (green arrows) of SAH (red) with the P1 helix (light blue). Distances for the electrostatic interaction are labeled. Atoms involved in the interactions are colored; oxygen is red and sulfur is yellow (PDB ID: 3GX3). (c) The interaction (green arrows) of SFG (red) with the P1 helix (light blue). Distances for the electrostatic interaction are labeled. Atoms involved in the interactions are colored; oxygen is red and nitrogen is blue (PDB ID: 3GX2). (d) Density (orange mesh) about SAH (red) and SFG (red) contoured to 1 σ from the final $2F_o - F_c$ maps. (e) Side-by-side comparison of SAM, SAH, and SFG colored according to their normalized *B*-factors. SAH has only slightly higher *B*-factors in the main-chain moiety, while SFG shows much higher *B*-factors through its entire amino acid moiety and in the ribose sugar as well. The color bar at the bottom shows the scale.

Introducing G–C pairs at these positions produces a similar trend in SAM affinity. Altering both conserved A–U pairs to G–C pairs while preserving the purine–pyrimidine polarity (mutant A6G/U7C–A87G/U88C) results in an ~25-fold loss in binding affinity (Table 2). This is likely the result of the introduction of the exocyclic amines of the two guanosine residues, which introduce steric bulk and two partial positive charges. Moreover, altering the orientations of these pairs produces the same pattern of affinity loss for SAM as seen in the A–U series—that is, a transversion of the 7–87 pair has a greater affect on binding affinity than the 6–88 pair, and the double transversion displays affinity similar to the single 7–87 transversion mutant. Notably, the A6C/U7G–A87C/U88G double transversion has only a 2.6-fold greater affinity for SAM than the wild-type RNA has for SAH, suggesting that this mutation almost completely abrogates the electrostatic interaction (Table 2).

The identity and orientation of the base pairs in P1 have a significantly different influence on the binding affinity for SAH. Of the four mutants tested for SAH binding, all were found to have nearly equal affinity for SAH, regardless of the sequence composition of P1 (70–80 μM, Table 2). Therefore, in the absence of a positively charged sulfonium group, the ligand is no longer affected by the nature of the minor groove surface of the P1 helix. This is reflected in the value of $K_{d,REL}$(SAH/SAM) (Table 2), which reveals that the wild-type sequence not only has the greatest affinity for SAM but also has the greatest selectivity for SAM over SAH. Thus, these data clearly indicate that the conservation of the A6–U88/U7–A87 pairs serves to both maximize affinity and specificity for SAM.

To determine the extent of the structural effects of mutations to the A6–U88/U7–A87 pairs on the RNA–ligand complex, we have crystallized and solved the structure of the most deleterious mutation,

the A6C/U7G–A87C/U88G double transversion, in the presence of SAM (Table 1). To facilitate crystallization, we included the A94G/U34C variations that enhance crystallizability and resolution in the sequence. The crystals of this mutant diffracted X-rays to 2.95 Å, and the resulting data yielded a final model with good refinement statistics (R_{work} = 22.1% and R_{free} = 27.5%). As observed with SAH and SFG, SAM binds this mutant in a manner very similar to that observed in the wild-type structure, retaining the same hydrogen-bonding contacts with P3 and J1/2 (Fig. S8). Notably, the sulfonium ion maintains electrostatic contact with the minor groove face of the P1 helix although it is shifted more than 1 Å closer to the 2′-hydroxyl group on G7, outside coordinate error of the structure (Fig. 5; Table 1). However, it is notable that the electron density about the methionine moiety of SAM is weak, suggesting that repositioning the electrostatic interaction has deleterious effects on establishing hydrogen bonds between the ligand and RNA (Fig. 5b). Additionally, the normalized *B*-factors for the ligand are slightly higher than that of wild type (Fig. 5c), although the normalized *B*-factors for the two RNAs are similar (Fig. S9). We interpret this as an indication of a more disordered ligand in the binding pocket of the A6C/U7G–A87C/U88G mutant. A maximum likelihood superposition[35] of the four structures presented in this study has an rmsd of 0.11 Å (rmsd of a classical pairwise least-squares superpositioning of these structures is 0.89 Å). Together, these data reinforce the idea that the SAM-I riboswitch has a rigid binding pocket that does not adapt to form optimal contacts with alternative ligands.

The general importance of conserved electrostatic interactions in SAM binding

Along with a refinement of the RNA structure, interactions with ions, and ligand conformation in the *Tte*SAM-I riboswitch aptamer domain, this study demonstrates the importance of the RNA–sulfonium ion interaction in recognition and selectivity. The importance of this electrostatic interaction is echoed in two other SAM-responsive riboswitches whose structures are known.[10,11] In both SAM-II and SAM-III, the RNA presents at least one carbonyl group (along with a 2′-hydroxyl group in the case of SAM-III) to the sulfonium group[10,11] (Fig. 6a and b). Not only are these interactions crucial for increasing ligand affinity, they are, like SAM-I, likely important for selectivity against SAH as well.

Despite the obvious differences in chemical structure of proteins and RNAs, these two macromolecules appear to use similar strategies for selective SAM recognition. For example, structures of the RsrI DNA methyltransferase have been solved with SAM, SAH, and SFG.[36] The sulfonium ion forms an electrostatic interaction with backbone carbonyls critical for orienting the methyl group on SAM for attack; without it, the amino acid moiety of the ligand is displaced and affinity drops, allowing product to be released[36] (Fig. 6c). L-Isoaspartyl (D-aspartyl) O2 methyltransferase, which is involved in protein repair, makes use of the electrostatic interaction in a different manner.[37] SAM and SAH bind with equivalent affinities and take up equivalent positions,[37] but the binding of SAM is accompanied by conformational change distal from the

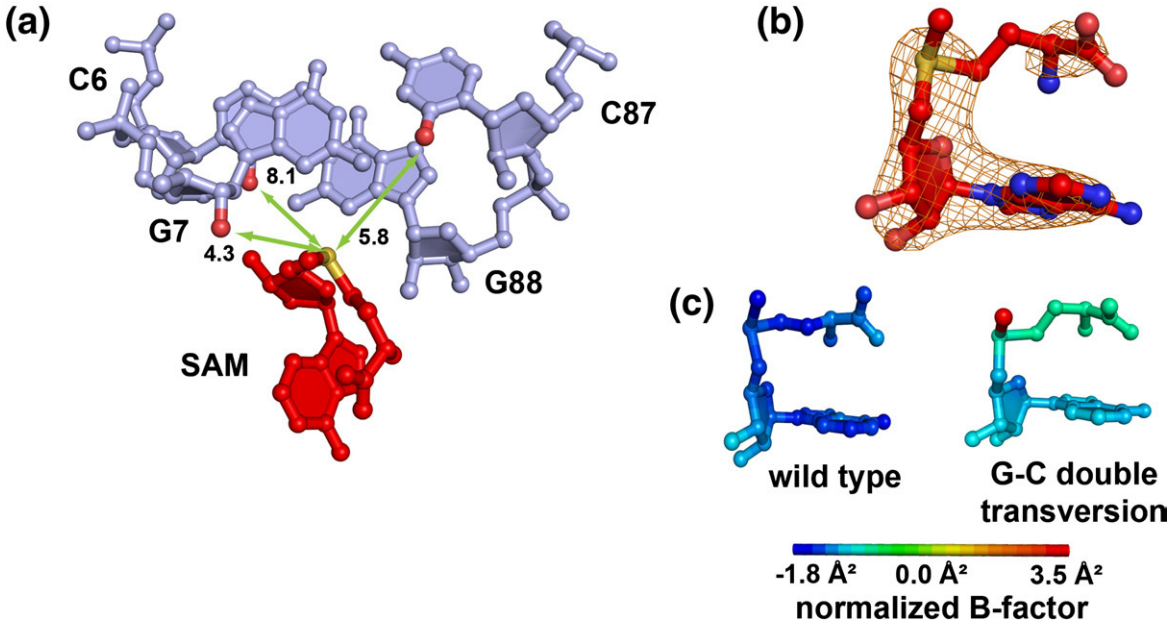

Fig. 5. (a) The interaction (green arrows) of SAM (red) with the P1 helix (light blue) in mutant A6C/U7G–A87C/U88G. Distances for the electrostatic interaction are labeled. Atoms involved in the interactions are colored; oxygen is red and sulfur is yellow (PDB ID: 3GX7). (b) Density (orange mesh) about SAM (red) contoured to 1 σ from the final $2F_o - F_c$ map. (c) Side-by-side comparison of SAM from *Tte*(A94G/U34C)SAM-I and mutant, colored according to their normalized *B*-factors. The SAM in the mutant RNA has higher *B*-factors overall, especially at the methyl group and through the methionine moiety. The color bar at the bottom shows the scale.

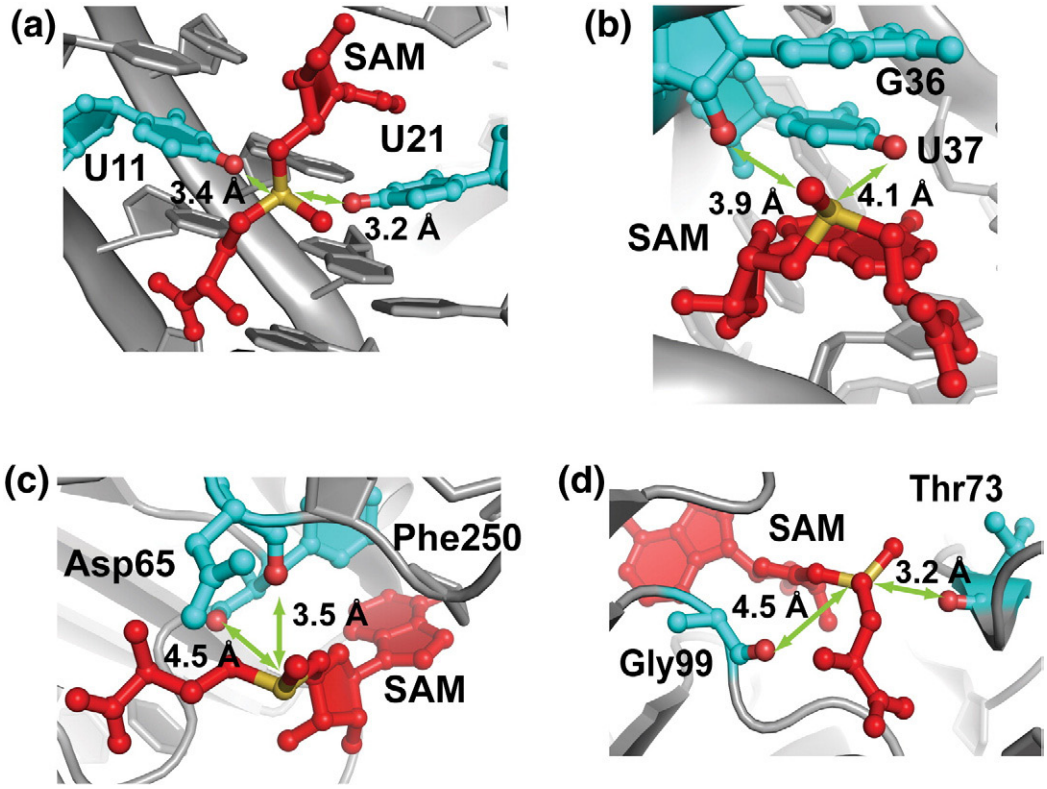

Fig. 6. Examples of electrostatic interactions (green arrows) in SAM-binding RNAs and proteins. SAM is red. Residues involved in the interactions are labeled and colored cyan; atoms involved are colored in the following manner: red is oxygen and yellow is sulfur. (a) SAM in the SAM-II riboswitch (PDB ID: 2QWY[11]). (b) SAM in the SAM-III riboswitch (PDB ID: 3E5C[10]). (c) SAM in the RsrI methyltransferase (PDB ID: 1NW5[36]). (d) SAM in the L-isoaspartyl (D-aspartyl) O2 methyltransferase (PDB ID: 1JG4[37]).

binding pocket, suggesting that the interaction formed by the SAM sulfonium with backbone carbonyls (Fig. 6d) drives a structural rearrangement in the protein.[37] In the case of the MetJ transcriptional repressor,[38] the electrostatics of SAM binding drive function but not through a conformational change to either the protein or the ligand itself. SAM binding increases the affinity of MetJ for its operator sequence by 250-fold when bound by changing the overall electrostatic potential of MetJ from net negative to positive, creating productive electrostatic interactions with the DNA.[39]

Interestingly, although the SAM-binding riboswitches fulfill similar regulatory functions as MetJ, the means by which they respond to SAM is more closely akin to the methyltransferases. In other words, among the riboswitches, the electrostatic interaction formed with SAM is coupled to a discrete conformational change either to the ligand, as seen in the SAM-III riboswitch and RsrI methyltransferase,[36] or to the macromolecule, as seen in the SAM-I riboswitch and the L-isoaspartyl methyltransferase.[37] These conformational changes play a key role in the function of these macromolecules. In the *Tte*SAM-I riboswitch, conformational change is thought to commit the riboswitch to a transcriptional off-state. Although SAH binds in the same manner as SAM, the lack of a strong interaction with the P1 helix prevents this stabilization, allowing formation of an alternative RNA conformation that commits the riboswitch to permitting full transcription of the mRNA and thereby gene expression. Not surprisingly, as both RNA and proteins have the same central constraint in their interactions with SAM along with a required need for selectivity against SAH, both classes of biological macromolecule utilize the same strategy in SAM recognition: an electrostatic interaction between the positively charged sulfonium ion and partial negative charges on carbonyl or hydroxyl groups. This study demonstrates that, as with proteins, the SAM-I riboswitch couples this electrostatic interaction to function.

Methods and Materials

Design and synthesis of variants

Crystal lattice contacts were identified using CNS[40] to generate symmetry mates of the refined structure (lattice contacts listed in Supplementary Table 1). Sequence mutations targeting these contacts were generated using standard PCR-mediated site-directed mutagenesis techniques using overlapping DNA primers.[41] RNAs containing mutations at the 6–88/7–87 pairs were prepared by PCR using forward primer and reverse primers that directly incorporated the desired changes, and the resulting fragment was inserted into plasmid vector pRAV12,[42] which bears a T7 promoter

upstream of the RNA sequence for transcription and an HδV ribozyme at the 3′ end of the RNA.

Preparation of the RNA

Transcription templates were prepared by PCR using primers directed against the T7 promoter and the HδV ribozyme in the DNA vector according to established methods.[42] RNA was transcribed *in vitro* according to previously described protocols, and the resulting products were purified by denaturing gel electrophoresis.[42] RNA was extracted from the gel by electroelution, exchanged three times into 10 mM Na^+-4-morpholineethanesulfonic acid at pH 6.0 and refolded by heating to 95 °C for 3 min followed by snap cooling on ice. The refolded RNA was exchanged once into 10 mM Na^+-4-morpholineethanesulfonic acid, pH 6.0, and 2 mM $MgCl_2$. Concentrations were assessed by absorbance at 260 nm using calculated extinction coefficients based upon nucleotide composition and a hypochromic effect correction factor of 1.3.

Crystallization, data collection, structural determination, and refinement

Immediately prior to crystallization, a 100-mM SAM stock in water was added to the 400-μM RNA stock in a 1:20 SAM:RNA (v/v) ratio for a final SAM:RNA molar ratio of 12.5:1. Sample and mother liquor were mixed at a 1:1 v/v ratio and crystals were grown by the hanging drop method at 30 °C. Depending on the construct, crystals grew to at least 100 μm on a side within 12 to 24 h. The optimal growth conditions varied slightly between constructs, but the typical conditions used were 12 mM spermine–HCl, 10% methyl-2,4-pentanediol (MPD), 40 mM Na^+-cacodylate, pH 7.0, 5–20 mM $BaCl_2$, and 60–80 mM KCl. The exact conditions for each construct tested are presented in Table S4. Crystals were cryoprotected by soaking in crystallization solution supplemented with 15% ethylene glycol for at least 5 min and flash-frozen in liquid nitrogen.

Due to refinement issues in the crystals grown in barium, magnesium was used as a divalent in most of the structures presented herein. For the final, higher-resolution data set, the crystals were grown in 40 mM Na^+-cacodylate, pH 7.0, 20 mM $MgCl_2$, 80 mM KCl, 8% MPD, and 16 mM spermine–HCl. The exact conditions in which other crystals reported in this work were grown are given in Table S4. The crystals of the A6C/U7G–A87G/U88C mutant complexed with SAM only grew in the presence of barium. To exchange this cation for magnesium, we washed these crystals three times with a solution composed of 2.5 mM SAM, 15 mM $MgCl_2$, 30 mM KCl, 40 mM Na^+-cacodylate, pH 7.0, 10% MPD, and 12 mM spermine–HCl. Five microliters of this solution was then added to the crystals, the well solution was replaced with the magnesium solution, and the crystals were allowed to soak for 2 h at 30 °C and then cryoprotected as described above. This exchange of barium for magnesium yielded crystallographic data that could be readily refined.

Crystals were screened for quality on a copper rotating anode source (Rigaku RU200 and Rigaku RU2HR) with a Rigaku MSC IV++ area detector at 100 K. Preliminary analysis was performed using D*TREK packaged as CrystalClear.[43,44] All crystallographic data and refinement statistics are presented in Table 1. The best of these variants, A94G/U34C, was used for collection of a high-resolution data set at the National Synchrotron Light Source at Brookhaven on beamline X29 equipped with a Q315 CCD detector. Data were scaled and averaged using HKL2000[45] (Table 1). The original SAM-I structure [Protein Data Bank (PDB) ID: 2GIS] was used as a search model in molecular replacement using PHENIX.[46] Diffraction anisotropy was corrected for in the A94G/U34C and manganese derivative data sets using the Diffraction Anisotropy Server at University of California, Los Angeles.[47] Density maps were calculated using PHENIX, and altered residues, metal ions, and waters were modeled using Coot[48] during iterative rounds of refinement using the simulated annealing, energy minimization, TLS refinement, individual atomic-displacement-factor refinement, and water-picking routines packaged in PHENIX.[46] The metal derivative, SAH, SFG, and A6C/U7G–A87G/U88C data sets were all collected in-house in the manner described previously and the structures were solved as described above.

Isothermal titration calorimetry

RNA was dialyzed overnight against 1 L of buffer consisting of 50 mM K^+–Hepes, pH 7.5, 100 mM KCl, and 10 mM $MgCl_2$. SAM was prepared through the dilution of a 100-mM stock using the same buffer used for dialysis of the RNA. SAH was prepared by dissolving dry SAH in the dialysis buffer. SAM and SAH concentrations were found using an extinction coefficient 15,400 M^{-1} cm^{-1} at 260 nm.[49] The RNA was in the sample cell and the ligands were in the syringe. To ensure that we were not measuring heats of dilution, titrations of SAH solution at the working concentration for the experiments were carried out into buffer (Supplementary Materials; Fig. S7) and the results were subtracted from the data obtained from titrating SAH into RNA using the Origin ITC software from MicroCal.[50] RNA concentrations were typically 10 μM for the tighter binding mutants and 25–50 μM for the weaker binders and SAH titrations to ensure a *c*-value between 0.5 and 140.[51–54] Measurements for determining SAM-binding affinities were taken using a 1:10 RNA:ligand ratio at a reference power of 5 μcal/s and temperature of 30 °C with thirty-two 10-μL injections at an injection rate of 0.5 μL/s with 240-s intervals. The SAH titrations were carried using a 1:10 RNA:ligand ratio at a reference power of 5 μcal/s and temperature of 30 °C with twenty-one 15-μL injections at an injection rate of 0.5 μL/s at 240-s intervals. These higher injection volumes were used to counter the problems encountered when performing ITC experiments at low values of *c*.[52,53]

Data collected were fit to a single-site binding model using the Origin ITC software from MicroCal.[50] Values of *n*, K_a (M^{-1}), ΔH (cal mol^{-1}), and ΔS (cal mol^{-1} K^{-1}) were extrapolated using the equation

$$q = v(\Delta H)[\mathrm{RNA}]\left(\frac{K_a[L]_i^n}{1 + K_a[L]_i^n} - \frac{K_a[L]_{i-1}^n}{1 + K_a[L]_{i-1}^n}\right) \quad (2)$$

where q is the heat released, v is the known volume of the reaction, K_a is the association constant, and L_i is the ligand concentration at the ith injection.[50] The disassociation constant K_d (M) was determined by taking the inverse of K_a. Each titration was carried out at least in triplicate. For the weaker-affinity systems, such as the GC double transversion mutant in the SAH experiment, the n value was fixed because the *c*-value was low[51–53] and the stoichiometry of the system is known.[5,9,13] The reported K_d values are the average of these repeated titrations and the reported error is the standard deviation.

Accession numbers

Coordinates and structure factors have been deposited in the PDB with accession numbers 3GX5 [*Tte*(U34C/A94G)SAM-I], 3GX6 ($MnCl_2$ derivative), 3GX3 (SAH), 3GX2 (SFG), and 3GX7 (A6C/U7G–A87G/U88C mutant).

Acknowledgements

The authors would like to thank Annie Héroux at the National Synchrotron Light Source in Brookhaven, NY, for her generous assistance in collecting the crystallographic data presented in this work. We would also like to thank members of the Batey laboratory for their critical comments and discussion in the preparation of the manuscript. This work was funded by National Institutes of Health grant GM-083953 (R.T.B.) and by a National Institutes of Health Pre-doctoral Training Grant in Molecular Biophysics (T32 GM-065103) (to R.K.M.).

Supplementary Data

Supplementary data associated with this article can be found, in the online version, at doi:10.1016/j.jmb.2009.12.007

References

1. Winkler, W. C. (2005). Riboswitches and the role of noncoding RNAs in bacterial metabolic control. *Curr. Opin. Chem. Biol.* **9**, 594–602.
2. Wang, J. X. & Breaker, R. R. (2008). Riboswitches that sense *S*-adenosylmethionine and *S*-adenosylhomocysteine. *Biochem. Cell Biol.* **86**, 157–168.
3. Epshtein, V., Mironov, A. S. & Nudler, E. (2003). The riboswitch-mediated control of sulfur metabolism in bacteria. *Proc. Natl Acad. Sci. USA*, **100**, 5052–5056.
4. McDaniel, B. A., Grundy, F. J., Artsimovitch, I. & Henkin, T. M. (2003). Transcription termination control of the S box system: direct measurement of *S*-adenosylmethionine by the leader RNA. *Proc. Natl Acad. Sci. USA*, **100**, 3083–3088.
5. Winkler, W. C., Nahvi, A., Sudarsan, N., Barrick, J. E. & Breaker, R. R. (2003). An mRNA structure that controls gene expression by binding *S*-adenosylmethionine. *Nat. Struct. Biol.* **10**, 701–707.
6. Corbino, K. A., Barrick, J. E., Lim, J., Welz, R., Tucker, B. J. & Puskarz, I. (2005). Evidence for a second class of *S*-adenosylmethionine riboswitches and other regulatory RNA motifs in alpha-proteobacteria. *Genome Biol.* **6**, R70.
7. Fuchs, R. T., Grundy, F. J. & Henkin, T. M. (2006). The S(MK) box is a new SAM-binding RNA for translational regulation of SAM synthetase. *Nat. Struct. Mol. Biol.* **13**, 226–233.
8. Weinberg, Z., Regulski, E. E., Hammond, M. C., Barrick, J. E., Yao, Z., Ruzzo, W. L. & Breaker, R. R. (2008). The aptamer core of SAM-IV riboswitches mimics the ligand-binding site of SAM-I riboswitches. *RNA*, **14**, 822–828.
9. Montange, R. K. & Batey, R. T. (2006). Structure of the *S*-adenosylmethionine riboswitch regulatory mRNA element. *Nature*, **441**, 1172–1175.
10. Lu, C., Smith, A. M., Fuch, R. T., Ding, F., Rajashankar, K., Henkin, T. M. & Ke, A. (2008). Crystal structure of the SAM-III/SAM(MK) riboswitch reveal the SAM-dependent translation inhibition mechanism. *Nat. Struct. Mol. Biol.* **15**, 1076–1083.
11. Gilbert, S. D., Rambo, R. P., VanTyne, D. & Batey, R. T. (2008). Structure of the SAM-II riboswitch bound to *S*-adenosylmethionine. *Nat. Struct. Mol. Biol.* **15**, 177–182.
12. Ueland, P. M. (1982). Pharmacological and biochemical aspects of *S*-adenosylhomocysteine and *S*-adenosylhomoecysteine hydrolase. *Pharmacol. Rev.* **34**, 223–253.
13. Lim, J., Winkler, W. C., Nakamura, S., Scott, V. & Breaker, R. R. (2006). Molecular-recognition characteristics of SAM-binding riboswitches. *Angew. Chem., Int. Ed. Engl.* **45**, 964–968.
14. Blount, K. F. & Breaker, R. R. (2006). Riboswitches as antibacterial drug targets. *Nat. Biotechnol.* **24**, 1558–1564.
15. Barrick, J. E. & Breaker, R. R. (2007). The distributions, mechanisms, and structures of metabolite-binding riboswitches. *Genome Biol.* **8**, R239.
16. Gilbert, S. D., Montange, R. K., Stoddard, C. D. & Batey, R. T. (2006). Structural studies of the purine and SAM binding riboswitches. *Cold Spring Harbor Symp. Quant. Biol.* **71**, 259–268.
17. Derewenda, Z. S. & Vekilov, P. G. (2006). Entropy and surface engineering in protein crystallization. *Acta Crystallogr., Sect. D: Biol. Crystallogr.* **62**, 116–124.
18. Yamada, H., Tamada, T., Kosaka, M., Miyata, K., Fujiki, S. & Tano, M. (2007). 'Crystal lattice engineering,' an approach to engineer protein crystal contacts by creating intermolecular symmetry: crystallization and structure determination of a mutant human RNase 1 with a hydrophobic interface of leucines. *Protein Sci.* **16**, 1389–1397.
19. Bauman, J. D., Das, K., Ho, W. C., Baweja, M., Himmel, D. M. & Clark, A. D. J. (2008). Crystal engineering of HIV-1 reverse transcriptase for structure-based drug design. *Nucleic Acids Res.* **36**, 5083–5092.
20. MacElrevey, C., Spitale, R. C., Krucinska, J. & Wedekind, J. E. (2007). A posteriori design of crystal contacts to improve the X-ray diffraction properties of a small RNA enzyme. *Acta Crystallogr., Sect. D: Biol. Crystallogr.* **63**, 815–825.
21. Juneau, K., Podell, E., Harrington, D. J. & Cech, T. R. (2001). Structural basis of the enhanced stability of a mutant ribozyme domain and a detailed view of RNA–solvent interactions. *Structure*, **9**, 221–231.
22. Guo, F. & Cech, T. R. (2002). Evolution of *Tetrahymena* ribozyme mutants with increased structural stability. *Nat. Struct. Biol.* **9**, 855–861.
23. Guo, F., Gooding, A. R. & Cech, T. R. (2004). Structure of the *Tetrahymena* ribozyme base triple sandwich and metal ion at the active site. *Mol. Cell*, **16**, 351–362.
24. Vicens, Q., Gooding, A. R., Laederach, A. & Cech, T. R. (2007). Local RNA structural changes induced by crystallization are revealed by SHAPE. *RNA*, **13**, 536–548.
25. Liu, J. & Lilley, D. M. J. (2007). The role of specific 2′-hydroxyl groups in the stabilization of the folded conformation of kink-turn RNA. *RNA*, **13**, 200–210.
26. Garst, A. D., Héroux, A., Rambo, R. P. & Batey, R. T. (2008). Crystal structure of the lysine riboswitch regulatory mRNA element. *J. Biol. Chem.* **283**, 22347–22351.
27. Serganov, A., Huang, L. & Patel, D. J. (2008). Structural insights into amino acid binding and gene control by a lysine riboswitch. *Nature*, **455**, 1263–1267.

28. Goody, T. A., Melcher, S. E., Norman, D. G. & Lilley, D. M. J. (2004). The kink-turn motif in RNA is dimorphic, and metal ion-dependent. *RNA*, **10**, 254–264.
29. Edwards, T. E. & Ferre-D'Amare, A. R. (2006). Crystal structures of the thi-box riboswitch bound to thiamine pyrophosphate analogs reveal adaptive RNA-small molecule recognition. *Structure*, **14**, 1459–1468.
30. Gilbert, S. D., Reyes, F. E., Edwards, A. L. & Batey, R. T. (2009). Adaptive ligand binding by the purine riboswitch in the recognition of guanine and adenine analogs. *Structure*, **17**, 857–868.
31. Thore, S., Frick, C. & Ban, N. (2008). Structural basis of thiamine pyrophosphate analogues binding to the eukaryotic riboswitch. *J. Am. Chem. Soc.* **130**, 8116–8117.
32. Yuan, Z., Zhao, J. & Wang, Z.-X. (2003). Flexibility analysis of enzyme active sites by crystallographic temperature factors. *Protein Eng.* **16**, 109–114.
33. Parasarathy, S. & Murthy, M. R. (1997). Analysis of temperature factor distribution in high-resolution protein structures. *Protein Sci.* **6**, 2561–2567.
34. Carugo, O. & Argos, P. (1998). Accessibility to internal cavities and ligand binding sites monitored by protein crystallographic thermal factors. *Proteins*, **31**, 201–213.
35. Theobald, D. L. & Wuttke, D. S. (2006). THESEUS: maximum likelihood superpositioning and analysis of macromolecular structures. *Bioinformatics*, **22**, 2171–2172.
36. Thomas, C. B., Scavetta, R. D., Gumport, R. I. & Churchill, M. E. (2003). Structures of liganded and unliganded RsrI N6-adenine DNA methyltransferase: a distinct orientation for active cofactor binding. *J. Biol. Chem.* **278**, 26094–26101.
37. Griffith, S. C., Sawaya, M. R., Boutz, D. R., Thapar, N., Katz, J. E., Clarke, S. & Yeates, T. O. (2001). Crystal structure of a protein repair methyltransferase from *Pyrococcus furiosus* with its L-isoaspartyl peptide substrate. *J. Mol. Biol.* **313**, 1103–1116.
38. Shoeman, R., Redfield, B., Coleman, T., Greene, R. C., Smith, A. A., Brot, N. & Weissbach, H. (1985). Regulation of methionine synthesis in *Escherichia coli*: effect of metJ gene product and *S*-adenosylmethionine on the expression of the metF gene. *Proc. Natl Acad. Sci. USA*, **82**, 3601–3605.
39. Phillips, K. & Phillips, S. E. V. (1994). Electrostatic activation of *Escherichia coli* methionine repressor. *Structure*, **2**, 309–316.
40. Brunger, A. T., Adams, P. D., Clore, G. M., DeLano, W. L., Gros, P. & Grosse-Kunstleve, R. W. (1998). Crystallography & NMR system: a new software suite for macromolecular structure determination. *Acta Crystallogr., Sect. D: Biol. Crystallogr.* **54**, 905–921.
41. Zheng, L., Baumann, U. & Reymond, J. (2004). An efficient one-step site-directed and site-saturation mutagenesis protocol. *Nucleic Acids Res.* **32**, e115.
42. Kieft, J. S. & Batey, R. T. (2004). A general method for rapid and nondenaturing purification of RNAs. *RNA*, **10**, 988–995.
43. Pflugrath, J. W. (1999). The finer things in X-ray diffraction data collection. *Acta Crystallogr., Sect. D: Biol. Crystallogr.* **55**, 1718–1725.
44. Rigaku, C. (2002). CrystalClear: an integrated program for the collection and processing of area detector data.
45. Otwinowski, Z. & Minor, W. (1997). Processing of X-ray diffraction data collected in oscillation mode. *Methods Enzymol.* **276**, 307–326.
46. Adams, P. D., Grosse-Kunstleve, R. W., Hung, L. W., Ioerger, T. R., McCoy, A. J. & Moriarty, N. W. (2002). PHENIX: building new software for automated crystallographic structure determination. *Acta Crystallogr., Sect. D: Biol. Crystallogr.* **58**, 1948–1954.
47. Strong, M., Sawaya, M. R., Wang, S., Phillips, M., Cascio, D. & Eisenberg, D. (2006). Toward the structural genomics of complexes: crystal structure of a PE/PPE protein complex from *Mycobacterium tuberculosis*. *Proc. Natl Acad. Sci. USA*, **103**, 8060–8065.
48. Emsley, P. & Cowtan, K. (2004). Coot: model-building tools for molecular graphics. *Acta Crystallogr., Sect. D: Biol. Crystallogr.* **60**, 2126–2132.
49. Windholz, M., Budavari, S., Blumetti, R. & Otterbein, E., eds. (1983). *The Merck Index,* 10th edit. Merck & Co., Inc., Rahway, NJ.
50. MicroCal, LLC. (2003). VP-ITC Microcalorimeter User's Manual, MicroCal, LLC, Northampton, MA.
51. Turnbull, W. B. & Daranas, A. H. (2003). On the value of *c*: can low affinity systems be studied by isothermal titration calorimetry? *J. Am. Chem. Soc.* **125**, 14859–14866.
52. Tellinghuisen, J. (2007). Optimizing experimental parameters in isothermal titration calorimetry: variable volume procedures. *J. Phys. Chem. B*, **111**, 11531–11537.
53. Tellinghuisen, J. (2008). Isothermal titration calorimetry at very low c. *Anal. Biochem.* **373**, 395–397.
54. Wiseman, T., Williston, S., Brandts, J. F. & Lin, L. N. (1989). Rapid measurement of binding constants and heats of binding using a new titration calorimeter. *Anal. Biochem.* **179**, 131–137.